Inhibition of CdS photocorrosion by Al$_2$O$_3$ shell for highly stable photocatalytic overall water splitting under visible light irradiation

Xiaofeng Ning[a,b], Wenlong Zhen[a], Yuqi Wu[a,*], Gongxuan Lu[a,*]

[a] *State Key Laboratory for Oxo Synthesis and Selective Oxidation, Lanzhou Institute of Chemical Physics, Chinese Academy of Science, Lanzhou 730000, China*
[b] *University of Chinese Academy of Science, Beijing 100049, China*

A B S T R A C T

Efficiency and stability are the two key points for CdS photocatalyst because its application has been seriously restricted owing to serious photocorrosion issue and the recombination of photo-induced charge pairs. In this paper, CdS nanoparticles (NPs) were surface-modified by chemical inert Al$_2$O$_3$ shell. This modification could prevent nascent formed oxygen induced photo-corrosion and enhance the photo-stability of CdS during water splitting significantly. In addition, it was found that such a shell could enhance efficient separation of photo-induced charge pairs. Besides, with the assistance of artificial gill of removing nascent formed O$_2$ from water, Pt/CdS@Al$_2$O$_3$ photocatalyst can achieve overall water splitting under visible light irradiation. The rate of H$_2$ evolution increased 126 times over Pt/CdS@Al$_2$O$_3$ composite compared with pure CdS NPs, and the stability was maintained in several cycles of reaction without any decrease. The measurement of concentration of Cd^{2+} in solution after long cycles by ICP method confirmed this anti-photo-corrosion property of Al$_2$O$_3$ shell on CdS. This work provides a new potential way to design and fabricate more stable and efficient CdS-based nanocomposite photocatalysts for versatile solar energy conversion.

1. Introduction

Solar light driven overall water splitting is a highly promising pathway towards a clean and renewable energy supply in the future [1–12]. The key issue of photocatalytic generation of hydrogen from water is dependent on the development of efficient and stable photocatalyst, which is able to accomplish overall water splitting under visible light irradiation without using sacrificial agents. Domen and co-workers [13] prepared a core/shell SiO$_2$/ Ta$_3$N$_5$ photocatalyst modified with spatially separated Pt nanoparticles (NPs) and IrO$_2$ NPs cocatalysts, which showed significantly enhanced water reduction and oxidation activity under visible light irradiation. C$_3$N$_4$ is also a potential candidate catalyst for water splitting when Pt and Co$_3$O$_4$ are fabricated onto the surface of hollow C$_3$N$_4$ spheres [14]. By effectively suppressing the recombination of carriers through spatial charge and decreasing the defect density, MgTa$_2$O$_{6-x}$/TaON heterostructure showed a high AQE of 6.8% of hydrogen evolution at 420 nm in Z-scheme overall water splitting [15]. Nevertheless, in spite of extensive efforts for overall water splitting, it still remains challenging to find a photocatalyst that exhibits adequate photon absorption, efficient charge separation, while showing stable activity to catalyze two half-reactions for hydrogen and oxygen generation. CdS, is a classical II–VI semiconductor with a band

gap of ca. 2.4 eV [16], offering a very good absorption to visible light in solar irradiation, has a suitable band position perfectly satisfying the thermodynamic requirements for water splitting [17–19]. Unfortunately, serious photocorrosion and rapid recombination of charge carriers in CdS [20–22] limit CdS applications in light driven reaction. Therefore, solving the photocorrosion and improving separation efficiency of photogenerated pairs in CdS are the main tasks to enhance its photocatalytic performance for overall water splitting.

Recently, extensive efforts have been paid in overcoming those CdS drawbacks, some of significant achievements have been fulfilled by controlling synthesis of CdS, for example, increasing of the surface area [23], tuning crystal sizes and structure (CdS nanowires (NWs), NPs, netted sphere-like CdS nanostructures), and synthesis of solid solution complex catalyst [24,25]. The solid solution is considered as an efficient way to improve the activity and stability of CdS based catalyst [26–29]. In addition, coupling CdS with other semiconductors is an effective method to suppress recombination of the photo-induced charge pairs, by coating with TiO$_2$ [30], ZnO [31], ZnS [32], WO$_3$ [33], PdS [34], Ag$_2$S [35]. However, most of the aforementioned materials are also easy photo-corroded, and the secondary formed metal ions are toxic or harmful to the environment and human health. Al$_2$O$_3$, as an earth-abundant and stable metal oxide [36,37], has been widely applied as

supporter material in catalysis with excellent chemical inertness [38–40]. It has been reported that Al_2O_3 could also enhance the charge transfer over g-C_3N_4/Al_2O_3 in the photocatalytic process [37]. If Al_2O_3 is successfully fabricated onto CdS surface, forming core–shell structure, the photogenerated hole oxidation of CdS would be prevented. In addition, due to the chemical inertness of Al_2O_3 shell, CdS would not be oxidized by the nascent formed oxygen dissolved in the water.

In this paper, we fabricated a thin shell of chemical inertness Al_2O_3 on the surface of CdS, and found that it could improve the photo-induced stability of CdS. In addition, it also could lead to efficient separation of photo-induced electrons and holes. Besides, by using an artificial gill in the photocatalytic overall water splitting system, we could efficiently remove newly dissolved oxygen to prevent the oxygen leading photocorrosion and inhibit the backward reaction of hydrogen and oxygen. The visible light induced overall water splitting by CdS has been achieved and the satisfied stability and photocatalytic activity in multi-cycle reaction have accomplished. This work can provide instructive guidance toward protecting the photosensitive semiconductors from photocorrosion, to design and prepare more stable and efficient catalyst for versatile solar energy conversion.

2. Experimental section

2.1. Materials

All chemicals were commercial purchased and used without further purification. Cadmium acetate ($Cd(CH_3COO)_2·2H_2O$, Sinopharm Chemical Reagent Co., Ltd, AR, ≥98.5%), sodium sulfide ($Na_2S·9H_2O$, Chengdu Kelong Chemical Reagent Co., Ltd, AR, ≥98.0%), aluminum nitrate nonahydrate ($Al(NO_3)_3·9H_2O$, Tianjin Kemiou Chemical Reagent Co., Ltd, AR, ≥99.0%), chloroplatinic acid, ($H_2PtCl_6·6H_2O$, Tianjin Kemiou Chemical Reagent Co., Ltd, AR, ≥99.0%), hydrazine hydrate ($H_4N_2·H_2O$, Xilong Chemical Co., Ltd., AR, >80%), sodium sulfate (Na_2SO_4, Xilong Chemical Co., Ltd., AR, >99%) are used as provided. Deionized water was used in the synthesis and reaction.

2.2. Preparation of CdS NPs sample

CdS NPs was prepared by a typical precipitation method at room temperature. Briefly, 0.46 g $Cd(CH_3COO)_2·2H_2O$ was dissolved in 200 mL of deionized water and stirred vigorously for 60 min, 0.83 g $Na_2S·9H_2O$ was dissolved into another 100 mL of deionized water by ultrasonication to obtain the Na_2S solution. Then the Na_2S solution was slowly added into the above-mentioned $Cd(CH_3COO)_2$ solution in a drop-by-drop process under vigorous stirring. After stirring for 3 h, the obtained products were separated by filtration and washed with deionized water several times, followed by a dry process at 353 K in vacuum oven.

2.3. Preparation of CdS@Al₂O₃ photocatalyst

In a typical preparation, 0.20 g CdS was uniformly dispersed into 200 mL of distilled water under constant magnetic stirring for 1 h. Subsequently, a known amount of $Al(NO_3)_3$ (the weight ratios of Al_2O_3 to CdS were controlled to be 0.5, 1.0, 2.0, 5.0 wt%) solution was added dropwise to the above suspension, followed by the addition of aqueous NH_3 (to attain pH ~8) and the fully mixed solution was stirred at room temperature for additional 2 h. After stirring, the prepared wet solution was dried at 373 K. The dried powder was calcined at 473–573 K for 2–6 h under a flow air to obtain efficient CdS@Al_2O_3 composites photocatalysts.

2.4. Preparation of Pt/CdS@Al₂O₃ photocatalyst

The platinization of Pt/CdS@Al_2O_3 was prepared by a typical hydrazine hydrate reduction method. 0.20 g as-prepared CdS@Al_2O_3 sample with a known amount of H_2PtCl_6 solution was stirred in 30 min, then hydrazine hydrate was dropped into the solution. Finally, the products were filtrated, rinsed with deionized water, and dried at 353 K to obtain the Pt/CdS@Al_2O_3 photocatalysts. The amount of Pt (the weight ratio of Pt to CdS@Al_2O_3) was controlled to be 0.5 wt%. In this paper, Pt/CdS@Al_2O_3 refers to the catalyst prepared under optimal condition (loading 1.0.wt% Al_2O_3 with $Al(NO_3)_3$ as a precursor).

2.5. Characterization of the catalysts

The powder X-ray diffraction patterns (XRD) of the samples were recorded on a Rigaku B/Max-RB X-ray diffractometer with a nickel-filtrated Cu Kα radiation in the 2θ ranging from 10 to 80° and a position sensitive detector using a step size of 0.017° and a step time of 15 s at 40 mA and 40 kV. X-ray photoelectron spectroscopy (XPS) analysis was performed using a VG Scientific ESCALAB 250Xi-XPS photoelectron spectrometer with an Al Kα X-ray resource. The binding energies were calibrated by the C1 s binding energy of 284.7 eV. The specific surface areas of the catalysts were determined by N_2 adsorption–desorption measurements by employing the Brunauer-Emmet-Teller (BET) method (Micromeritics apparatus ASAP 2020 M) at 77 K. Transmission electron microscopy (TEM) and HRTEM images were taken with a Tecnai-G2-F30 field emission transmission electron microscope operating at accelerating voltage of 300 kV. Elemental mapping was performed by using an energy-dispersive X-ray spectrometer (EDS) attached to the TEM instrument. Ultraviolet–visible (UV–vis) diffuse reflectance spectra (DRS) were obtained with a Hewlett-Packard 8453 spectrophotometer in which $BaSO_4$ powder was used as the internal standard to obtain the optical properties of the samples. The photolumi-nescence (PL) spectra for samples were investigated on an Edinburgh FL/FS900 spectrophotometer with an excitation wavelength of 420 nm. The inductively coupled plasma-optical emission spectrometer (ICP) was performing on Agilent 725-ES unit. The ICP signal intensities were calibrated by using a Cd elemental ICP standard solution.

2.6. Artificial gill [41]

It is known that fish can extract the dissolved oxygen from the water through the gill. Gill is a typical respiratory organ of fish, which consists of gill arch, gill rake, gill filament, gill lamella, etc. Fish exchanges the gas by gill lamella in the water. Gill wall is very thin, and contains a lot of capillaries. In the gills, the dissolved oxygen in the water is first absorbed by the capillaries, and the carbon dioxide is exchanged into the water in the meantime. One can achieve similar function just using a gas diffusion polymer film, one side is water with dissolved oxygen and another side is bubbled with high pure argon gas. By this way, the oxygen concentration difference leads to oxygen diffusion from water side to the gas side, then the dissolved oxygen in water could be transferred from reaction mixture to gas phase. We apply artificial gill to the photocatalytic overall water splitting system by a set of polymer film in the catalyst dispersion. The continuous argon gas was injected to gas side to decrease oxygen concentration in gas side of separation membrane, thus the dissolved oxygen in water would penetrate the separation membrane to gas side and was moved out of the reaction system. The structure of fish gill and the schematic diagram of photocatalytic reaction system are in Fig. S1.

2.7. Photocatalytic H₂ evolution activity

Photocatalytic experiments were performed at room temperature in a sealed Pyrex flask (212 mL) with a flat window (an efficient irradiation area of 9.8 cm²) and a silicone rubber septum for sampling. 100 mg of catalyst was dispersed into 150 mL H_2O under the ultrasound treatment (25 kHz, 250 W) about 30 min. Prior to irradiation, the reactant mixture was degassed by bubbling Ar gas for 30 min. The Xenon lamp (HSX-UV 300) with a 420 nm cut-off filter was used as a light source to

trigger the photocatalytic reaction. The amount or rate of hydrogen evolution was measured using gas chromatograph (Agilent 6820, TCD, $13 \times$ columns, Ar carrier). A continuous magnetic stirrer was applied at the bottom of the reactor in order to keep the photocatalyst in suspension status during the whole experiment. Besides, in this study, the artificial gill was included in the Pt/CdS@Al$_2$O$_3$ reaction system for the water splitting reaction.

The apparent quantum efficiency (AQE) was measured under the same photocatalytic reaction conditions with irradiation light through a bandpass filter (430, 460, 490, 520, and 550 nm). Photon flux of the incident light was determined using a Ray virtual radiation actinometer (FU 100, silicon ray detector, light spectrum, 400–700 nm; sensitivity, $10–50 \, \mu V \, \mu mol^{-1} \, m^{-2} \, s^{-1}$). The reaction solutions were irradiated for 2 h with bandpass filters for AQE tests on the H$_2$ production. The following equation was used to calculate the AQE.

$$AQE = \frac{2 \times \text{the number of evolved hydrogen molecules}}{\text{the number of incident photos}} \times 100\%$$

The recycling test of photocatalytic H$_2$ evolution over the catalyst was done as follows. Typically, after the photocatalytic reaction of the first run under visible light irradiation, the photocatalytic system was thoroughly degassed again, without the separation of photocatalysts. Subsequently, the reactor was irradiated again by a 300 W Xe lamp with a 420 nm cut-off filter. Analogously, the following runs of photocatalytic recycling tests were performed.

2.8. Photocatalytic splitting D$_2$O and H$_2^{18}$O isotope-labeled experiments

The isotopes tracer experiments have been performed under downsizing the experimental conditions of photocatalytic splitting D$_2$O and H$_2^{18}$O. Typically, 10 mg catalyst dispersed in 10 mL D$_2$O or 2 mL H$_2^{18}$O in the sealed Pyrex flask. After ultrasonic treatment for 30 min, the suspended aqueous solution is degassed by bubbling Ar gas for another 40 min. After visible light irradiation for 6 h, the gas mixture in container was measured by GC–MS (Agilent Technologies, GC 7890A with a PONA capillary column (50 m × 0.20 mm × 0.50 μm), MS 5975C, the temperature of sample injector was maintained at 240 °C).

2.9. Photoelectrochemical performance

Photoelectrochemical experiments were carried out on an electrochemical workstation (CHI 660E). The electrochemical system consists of three electrodes with platinum sheet as a counter electrode and a saturated calomel electrode (SCE) as a reference electrode, along with the sample (1 cm × 1 cm) as a working electrode. 0.2 M aqueous Na$_2$SO$_4$ electrolyte solution without any additives was used in the reaction system. A 300 W Xe arc lamp equipped with a band-pass light filter ($\lambda > 420$ nm) was applied as light source. Mott–Schottky plots were measured at a different frequency without light illumination. The measured potentials vs. SCE were converted to the normal hydrogen electrode (NHE) scale by Eq. (1):

$$E_{NHE} = E_{SCE} + 0.24 \tag{1}$$

3. Results and discussion

3.1. Morphology analysis

The morphology of the catalysts was investigated using transmission electron microscopy (TEM) and high-resolution transmission electron microscopy (HRTEM). Fig. 1a shows the TEM image of the CdS NPs sample, which displays highly uniformly nanoparticles with diameter ca. 10 nm. The selected area electron diffraction (SAED) pattern in the inset of Fig. 1a indicates the polycrystalline structure nature of CdS. Fig. 1b shows the lattice spacing of 0.336 nm that can be assigned to the

(111) plane of the cubic CdS. In Fig. 1c, it can be clearly seen by the detailed TEM analysis of Pt/CdS@Al$_2$O$_3$ sample with the optimum photoactivity. It is obviously found that the CdS particle size slightly increases after at a high temperature treatment, and it remains polycrystalline structure from the SAED image in the inset of Fig. 1c. The HRTEM image showed that the CdS NP was covered by an Al$_2$O$_3$ shell, and this shell was in low-crystallinity or amorphous-similar state because there was no obvious lattice fringe of Al$_2$O$_3$ in the image [42,43]. The core–shell structure was in a uniform size of ~20 nm in Fig. 1d. Since the Pt content was very low (0.5 wt%), the size of Pt particles could not be determined from the HRTEM images. While the elemental mapping image (Fig. 1e) of Pt/CdS@Al$_2$O$_3$ nanocomposite distinctly exhibits that Cd, S, Al, O and Pt elemental spots relatively homogeneous within Pt/CdS@Al$_2$O$_3$. In addition, the Al elements are rather scattered over the CdS. In Fig. 1f the EDX data, it could also prove the presence of Cd, S, Al, O, and Pt in Pt/CdS@Al$_2$O$_3$ nanocomposite, implying the Pt/CdS@Al$_2$O$_3$ photocatalyst was successfully synthesized.
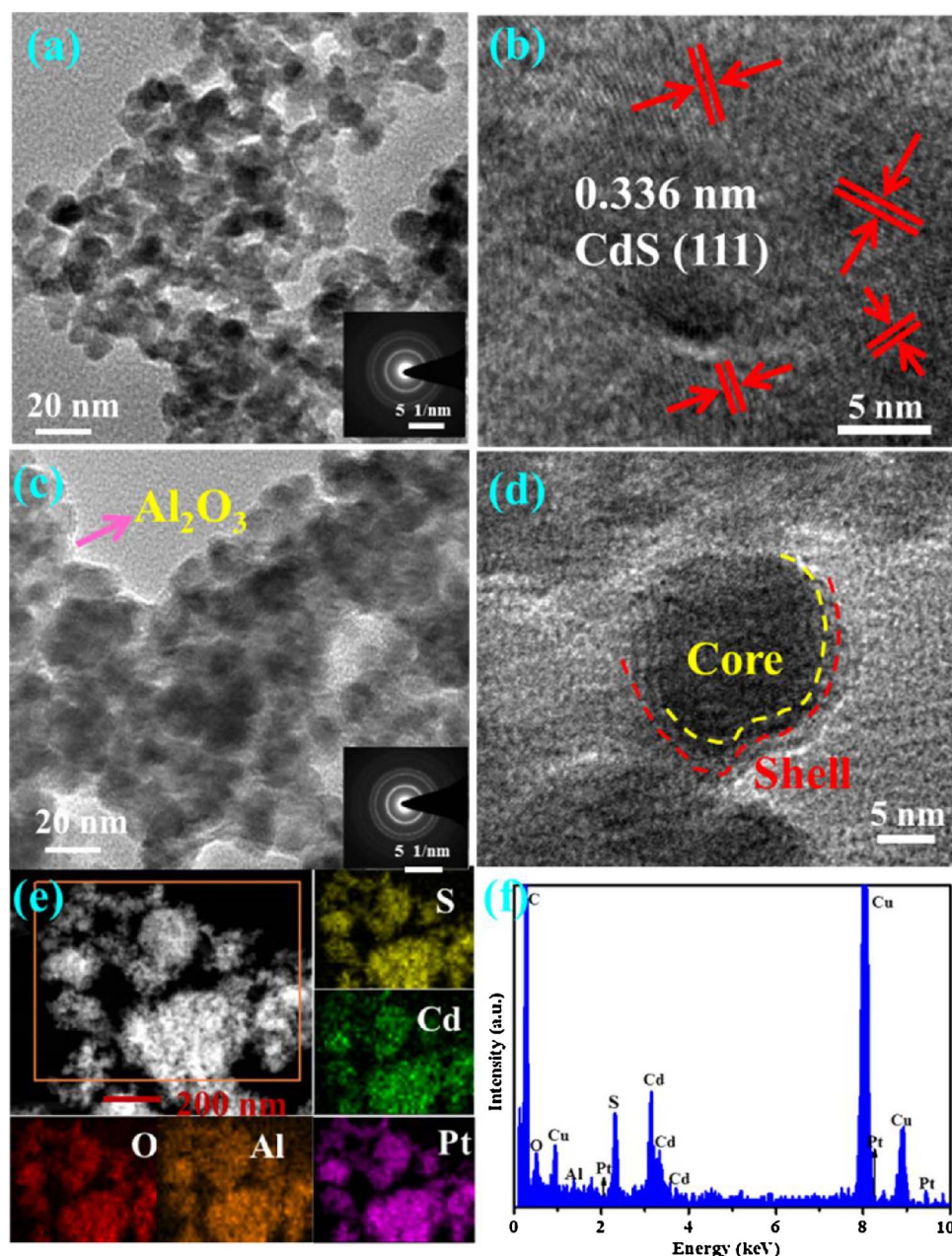
3.2. XRD analysis

The crystalline structure and phase composition of the prepared catalysts were analyzed by X-ray diffraction. Fig. 2 shows the XRD patterns of Pt/CdS@Al$_2$O$_3$ catalysts prepared by calcining the CdS@Al(NO$_3$)$_3$ precursor at various calcination conditions, along with the data of CdS for a comparison. The as-prepared CdS NPs can be ascribed to the type of cubic phase CdS [44,45]. The diffraction peaks at 26.5° (d = 3.355 Å), 43.9° (d = 2.055 Å) and 52.1° (d = 1.752 Å) can be assigned to the CdS cubic phase (111), (220), and (311) crystal planes, respectively. It is obviously found that the diffraction peaks are broad, which also implies the crystallite size of CdS nanoparticle is relatively small. Diffraction peaks corresponding to the cubic of CdS are present for all Pt/CdS@Al$_2$O$_3$ catalysts calcined at different conditions. With increasing the calcination time and temperature, the diffraction peaks become sharper and stronger, indicating the improvement of the CdS crystallinity and the growing of the crystal sizes. The result is in accordance with the TEM images. Further observation could be found that comparing to pure CdS NPs, the peak at 26.5° of Pt/CdS@Al$_2$O$_3$ gradually divides into three peaks with increasing the calcination time and temperature. This phenomenon may be due to the tendency of phase transformation from cubic to hexagonal under thermal treatment.

3.3. UV–vis spectra analysis

The UV–vis diffuse reflectance spectra (DRS) are used to analyze the optical properties of the samples. Fig. 3a displays that the shell Al$_2$O$_3$ out of CdS surface has an important impact on the optical property of light absorption for the as-prepared Pt/CdS@Al$_2$O$_3$ composite in the ultraviolet region. It is clear to see that the Pt/CdS@Al$_2$O$_3$ composite demonstrates enhanced light absorption capacity in the UV region, compared to pure CdS NPs. With the additional of Al$_2$O$_3$ covering with CdS exhibits enhanced absorption in UV light, which is understandable because Al$_2$O$_3$ its optical property has strong UV light absorption and low visible light absorption. As a semiconductor, the optical absorption near the band edge follows the formula $ah\nu = A(h\nu - Eg)^{n/2}$, where a, ν, Eg, and A are the absorption coefficient, light frequency, band gap energy, and a constant, respectively [46,47]. Moreover, n is a constant that depends on the characteristics of the transition in the semiconductor, namely, direct transition (n = 1) or indirect transition (n = 4). The optical transition for CdS was direct and the band gap energy of CdS and Pt/CdS@Al$_2$O$_3$ were estimated to be 2.28 and 2.34 eV, respectively. (in Fig. 3b). In addition, Fig. S2 shows the DRS spectra of Pt/CdS@Al$_2$O$_3$ composites annealed at various conditions. The shape and position of absorption edges did not change significantly [48].

Fig. 1. (a) TEM image and (b) HRTEM of CdS NPs, (c) TEM, (d) HRTEM and (e) EDX elemental mapping, and (f) EDX spectrum for Pt/CdS@Al$_2$O$_3$ composites, inset in panel a and c are the selected area electron diffraction (SAED) pattern.

3.4. BET surface areas and pore size distributions

The textural properties of the as-prepared samples were analyzed by nitrogen adsorption–desorption. Fig. 4a displays the nitrogen adsorption–desorption isotherms of CdS NPs and Pt/CdS@Al$_2$O$_3$ composites. According to their isotherms shapes, both of them correspond to type IV, indicating the presence of a mesoporous structure [49,50]. The isotherms of the catalysts exhibit H3 hysteresis loop related to the presence of ink-bottle pores with narrow necks and wider bodies [51]. The existence of mesopores can be further verified by the corresponding Barrett-Joyner-Halenda (BJH) pore size distribution curves (Fig. 4b). The CdS NPs pore diameter is lower than 10 nm, with maximum pore diameters around 6 nm. The Pt/CdS@Al$_2$O$_3$ composites exhibit a wide pore size distribution from 2 to 20 nm, which will provide efficient transport pathways for reactant and product molecules [52]. As shown in Table 1, it can be observed that coating Al$_2$O$_3$ thin shell onto the surface of CdS NPs can affect the surface area and porosity. The BET surface area and pore volume of CdS NPs are 111.9 m^{2}g^{-1} and

0.232 cm^3 g^{-1}, respectively, which are much larger than those of Pt/CdS@Al$_2$O$_3$ composites (57.5 m^2 g^{-1} and 0.199 cm^3 g^{-1}, respectively). The decrease in BET surface area and pore volume for Pt/CdS@Al$_2$O$_3$ composites may due to the calcination and the covering of support Al$_2$O$_3$ and Pt on the surface of CdS, which blocked some pores in CdS.

3.5. XPS analysis

The surface composition and chemical state of the Pt/CdS@Al$_2$O$_3$ composites were determined by XPS and the results were shown in Fig. 5. The most intense photoemission lines of Pt were those arising from the Pt 4f levels, and this energy region was overlapped by the presence of Al 2p peak, which resulted in the direct analysis of the platinum states very complicated. Therefore, we used a different line, Pt 4d was analyzed instead [53]. The survey spectra shown in Fig. 5a confirms the presence of Cd, S, Al, O and Pt in Pt/CdS@Al$_2$O$_3$ composites, which is in good agreement with the EDS results. As depicted in Fig. 5b, the Cd 3d spectrum exhibits two strong peaks at the binding
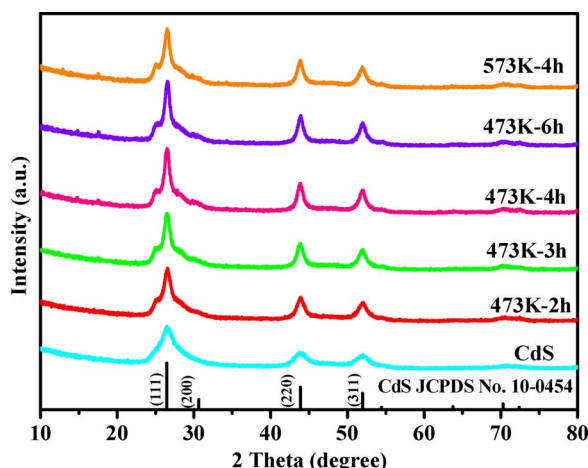
Fig. 2. The XRD patterns of Pt/CdS@Al$_2$O$_3$ calcined at 473 K for 2 h, 3 h, 4 h, 6 h and 573 K for 4 h in air atmosphere, along with prepared CdS for comparison.

energies of 405.1 and 411.8 eV, corresponding to the Cd 3d$_{5/2}$ and Cd 3d$_{3/2}$ peaks, respectively, which are the typical values of Cd^{2+} [54,55]. The S 2p spectrum (Fig. 5c) shows two peaks at 161.5 and 162.7 eV, which indicates that S is in the S^{2-} state [56–58]. Moreover, the peaks of Cd 3d and S 2p in Pt/CdS@Al$_2$O$_3$ composite have a slight shift to high energy direction compared to CdS NPs (in Fig. S3), which means Pt/CdS@Al$_2$O$_3$ composites with a more stable structure [56]. The clear Al 2p peak at 74.6 eV (Fig. 5d) can be ascribed to Al^{3+}. The binding energy of Al 2p, which shiftes toward a higher energy compared to pure Al$_2$O$_3$ [56,58], correspondingly, the binding energy of O1 s at 531.6 eV in Pt/CdS@Al$_2$O$_3$ was observed, indicating the O^{2-} state in Al$_2$O$_3$ (Fig. 5e) [37]. These results indicated that Al$_2$O$_3$ was closely over-coated on CdS surface and there was strong interaction between CdS and Al$_2$O$_3$ [37]. The Pt 4d lines were shown in Fig. 5f, the two peaks at ca. 315.7 and 332.7 eV were ascribed to Pt 4d$_{5/2}$ and Pt 4d$_{3/2}$ of metallic Pt, respectively, suggesting that the surface Pt species had been reduced to metallic Pt completely [59].

3.6. Photocatalytic activity

The photocatalytic tests of the as-prepared catalysts in a reactor equipped with an artificial gill assist were carried out under visible light irradiation (λ > 420 nm). Fig. S4 shows the rate of H$_2$ evolution on Pt/CdS@Al$_2$O$_3$ catalysts prepared by calcining the CdS@Al(NO$_3$)$_3$ precursor at different conditions. Clearly, with the increase of the calcination temperature and time, the activities increase and reach the highest value when the calcination temperature is at 473 K–4 h. The results indicate that calcination temperature and time may play an
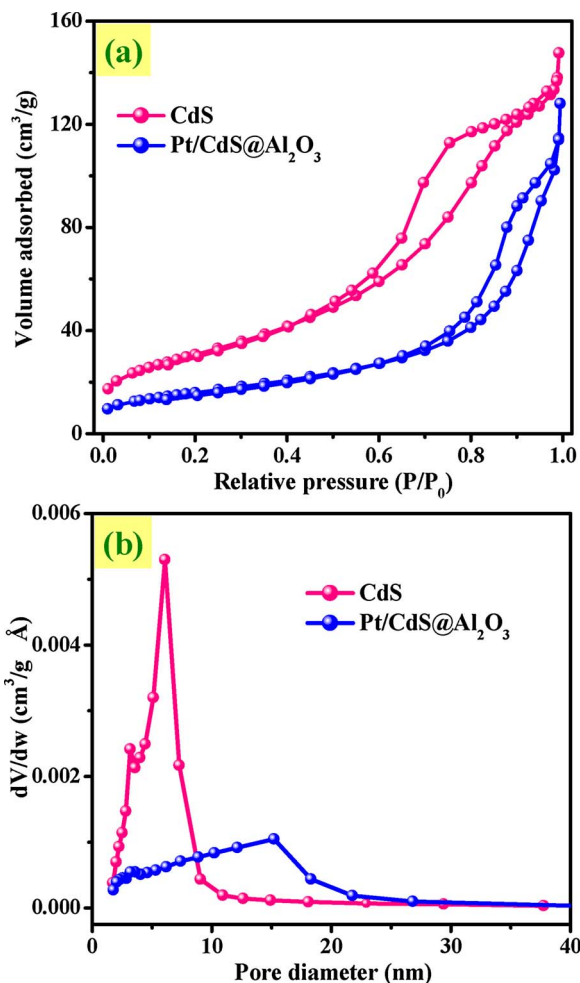

Fig. 4. (a) N$_2$ adsorption–desorption isotherms and (b) Barrett-Joyner-Halenda (BJH) pore size distributions of the as-prepared CdS NPs and Pt/CdS@Al$_2$O$_3$ composites.

Table 1
Summary of textural properties and photocatalytic activities of samples.

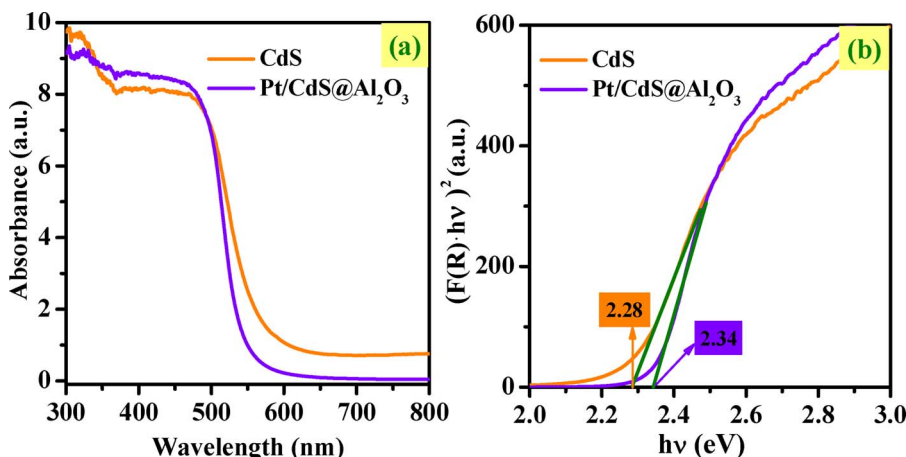| Sample	S_{BET} (m^2 g^{-1})	Pore volume (cm^3 g^{-1})	Average pore size (nm)	H$_2$ evolution rate (μmol h^{-1} g^{-1})
CdS	111.94	0.23	6.10	0.49
Pt/CdS@Al$_2$O$_3$	57.52	0.20	11.72	62.1

Fig. 3. (a) UV–vis diffuse reflection spectrum and (b) ahν–hν curve of the as-prepared CdS NPs and Pt/CdS@Al$_2$O$_3$ composites prepared by calcining the CdS@Al(NO$_3$)$_3$ at 473 K–4 h.
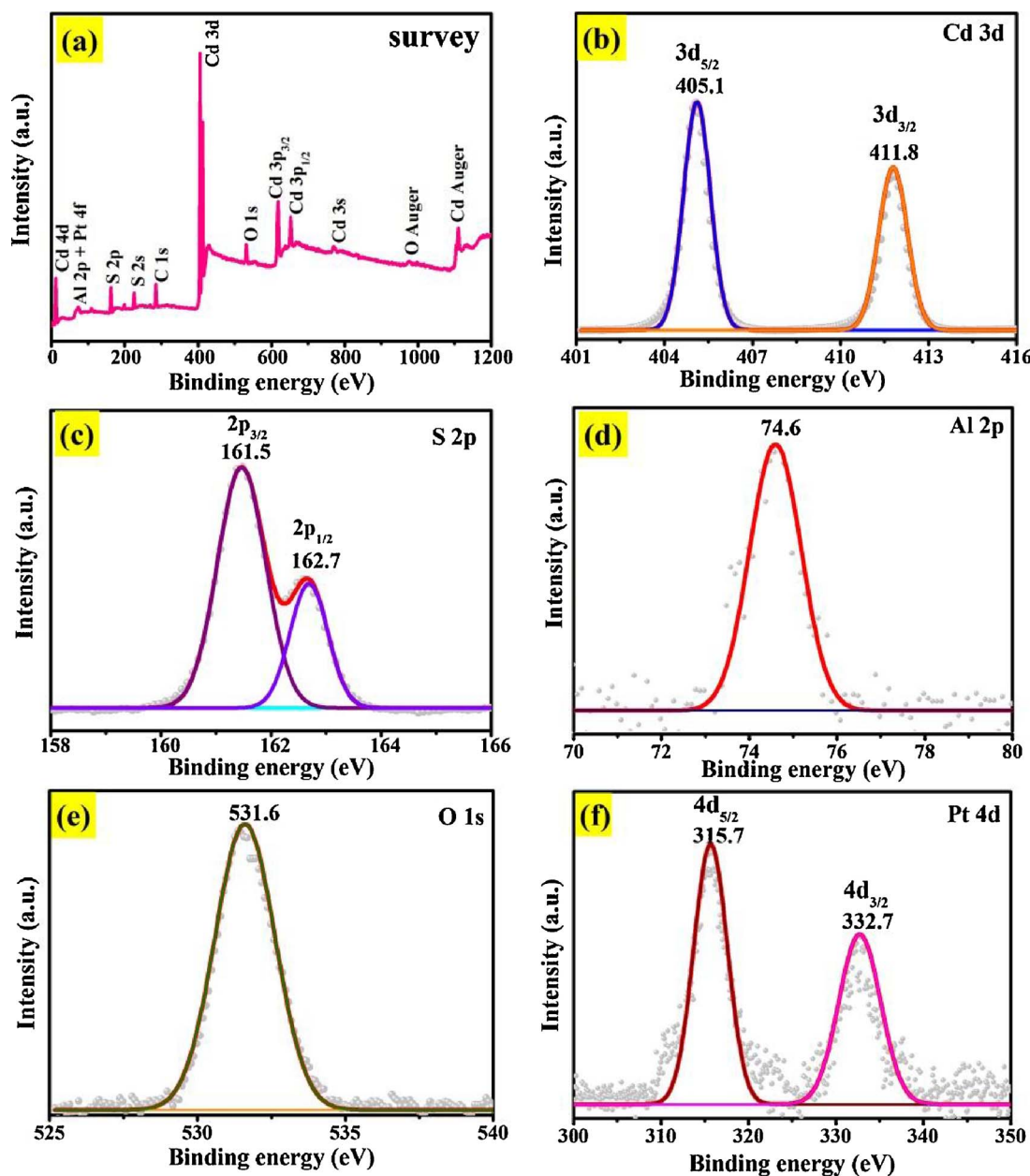
Fig. 5. The XPS spectra of Pt/CdS@Al$_2$O$_3$ composites (a) survey, (b) Cd 3d, (c) S 2p, (d) Al 2p, (e) O 1s, and (f) Pt 4d spectrum, respectively.

important role in the performance of Pt/CdS@Al$_2$O$_3$ composite. Generally, CdS can be oxidized to CdO and CdSO$_4$ when it is heated in the air at higher calcination temperature (> 573 K). For example, it was reported that CdS could be oxidized into CdO when it was annealed at 573–723 K in air [60–62], and this CdO would act as a photocatalytic activity inhibitor due to its more positive CB position than the redox potential of H$^+$/H$_2$ [63,64]. The temperature calcination of CdS in the air (at 773 K) will lead to oxidation of CdS and formation of sulfate (SO$_4{}^{2-}$) in Fig. S5. The existence of CdSO$_4$ will decrease the H$_2$ production amount (see Fig. S5d), might owing to decreasing visible light absorption of CdS by CdSO$_4$, reducing the generation of charge carriers and the photocatalytic performance [65,66]. Fig. S6 shows the effect of the amount of Al$_2$O$_3$ over Pt/CdS@Al$_2$O$_3$ on the H$_2$ evolution rate. The rate of H$_2$ evolution increases with increasing amount of Al$_2$O$_3$ from 0.5 to 1.0 wt%. However, further increasing the amount of Al$_2$O$_3$ leads to the decrease in the photocatalytic activity. Possibly, the thicker Al$_2$O$_3$ shell on the surface of CdS will prevent light penetration and absorption [67], resulting in the less photogenerated electrons and holes.

The catalyst lifetime is of great importance in the photocatalytic performance. The stability and reusability of CdS based catalysts were evaluated by the cycling hydrogen evolution experiment and the results were shown in Fig. 6. Due to the fast recombination of photogenerated charges and the shortage of activity sites in CdS NPs, bare CdS NPs presents a relatively low photocatalytic activity for hydrogen evolution, with a H$_2$ evolution rate of 0.49 µmol h^{-1}g^{-1}. Fig. S7 shows the photocatalytic cycling activity of blank CdS NPs, it is obviously found that the activity decreases significantly with the irradiation cycles, which is attributed to the quick photocorrosion of CdS. Notably, loading Al$_2$O$_3$ shell onto the surface of CdS NPs are capable of remarkably improving the rates of H$_2$ evolution. The average H$_2$ production rate reaches 62.1 µmol h^{-1}g^{-1} over Pt/CdS@Al$_2$O$_3$, such an activity is approximately 126 times higher than that of CdS NPs, compared favorably with the previously reported CdS-based heterostructure (Table S1). It is clearly seen that Pt/CdS@Al$_2$O$_3$ photocatalyst still exhibits excellent photocatalytic performance for water splitting even after 30 h irradiation. These results indicate that the as-prepared Pt/CdS@Al$_2$O$_3$
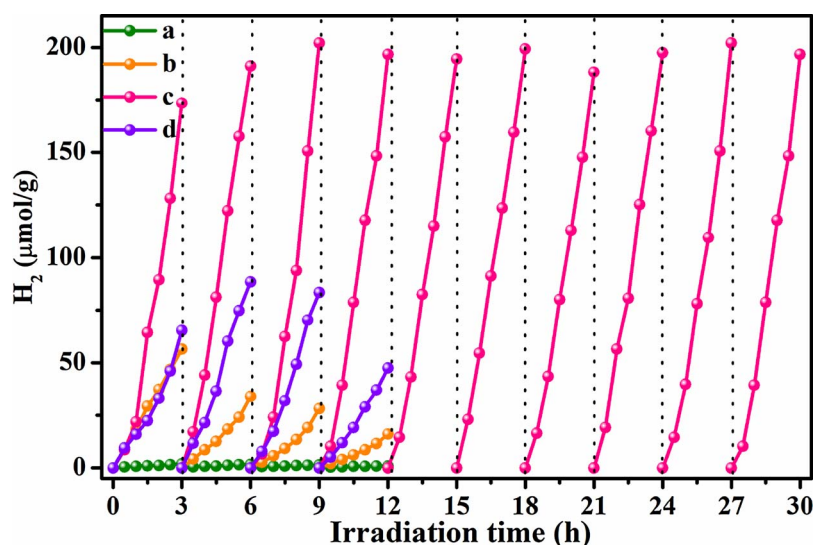
Fig. 6. Cycling runs for the photocatalytic hydrogen evolution activity under visible light over various samples: (a) CdS NPs, (b) Pt/CdS, (c) Pt/CdS@Al$_2$O$_3$ with artificial gill and (d) Pt/CdS@Al$_2$O$_3$ without artificial gill.
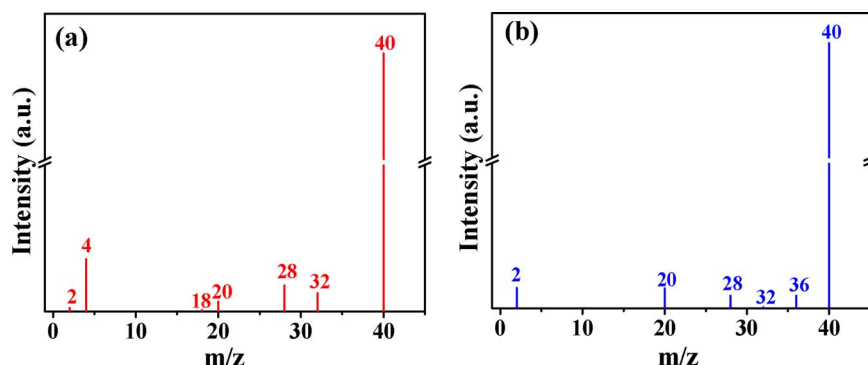

Fig. 7. GC–MS spectra obtained illumination 6 h toward photocatalytic splitting over Pt/CdS@Al$_2$O$_3$ photocatalyst (a) D$_2$O and (b) H$_2$^{18}O.

photocatalyst is a stable and efficient visible-light photocatalyst for water splitting under our reaction conditions. To testify the role of Al$_2$O$_3$ in Pt/CdS@Al$_2$O$_3$, the corresponding characterizations of Pt/CdS (in Fig. S8) and the photocatalytic performance have been carried out. It was obviously to find that the evolution rate gradually decreased with time over Pt/CdS. This result suggested that the photocorrosion of CdS caused the decrease of the activity of Pt/CdS [66]. Pt is a well-defined catalyst for the hydrogen evolution reaction, but it does not effectively avoid CdS corrosion in a sacrificial agent-free solution [68]. The results indicated that the enhancement of H$_2$ evolution reaction by the Al$_2$O$_3$ shell, which served as a stable oxide matrix to protect the embedded CdS particles from photocorrosion, and also implied that the Al$_2$O$_3$ would facilitate transfer of photogenerated electrons and holes in CdS [66]. In order to reveal the impact of artificial gill on the H$_2$ evolution in this reaction system, the photocatalytic activity of Pt/CdS@Al$_2$O$_3$ composite without utilization artificial gill was compared. Clearly, Pt/CdS@Al$_2$O$_3$ photocatalyst showed comparatively low activity in the absence of artificial gill, and the stability was low as well. Here, the artificial gill can not only remove newly formed O$_2$ from water to prevent the oxygen leading photocorrosion, but inhibit the hydrogen and oxygen back recombination to water. In this reaction system, no sacrificial agent was added. We calculated the formed O$_2$ and results were presented in Fig. S9. The Pt/CdS@Al$_2$O$_3$ composite could achieve overall water splitting into H$_2$ and O$_2$ with the approximate mole ratio (2:1).

In the recent reports [69–71], it has demonstrated the activation energy of H$_2$ and O$_2$ recombination reaction is 16.5 kJ/mol whether under irradiation or not. This backward reaction in overall water splitting is a thermal catalytic process and the H$_2$ and O$_2$ can easily recombine without too much extra energy barrier, which will result an

unfavourable effect in hydrogen evolution. In order to further elaborate the backward reaction of H$_2$ and O$_2$ forming H$_2$O in Pt/CdS@Al$_2$O$_3$ dispersion, the H$_2$ and O$_2$ recombination experiment was performed. As shown in Fig. S10, the reactor was injected stoichiometric H$_2$ and O$_2$, the detected H$_2$ decreased significantly with reaction time, indicating the occurrence of H$_2$ and O$_2$ recombination reaction. Hence, separating the formed H$_2$ and O$_2$ from the reaction system is one of the key factors to realize high efficiency of overall water splitting. The artificial gill could remove the nascent formed O$_2$ dissolved in the water out of the reactor to achieve high efficiency of overall water splitting.

3.7. Isotopes tracer experiments, ICP and AQE analysis

To further confirm that H$_2$ and O$_2$ were simultaneously generated via water splitting over Pt/CdS@Al$_2$O$_3$ catalyst, the isotopic tracer experiments were carried out. As displayed in Fig. 7a, the *m/z* signal at 4 corresponded to the D$_2$, thus indicating that the D$_2$ could be generated by photocatalytic splitting D$_2$O, meanwhile, in Fig. 7b, the detected *m/z* signal at 36 was corresponding to the ^{18}O$_2$, that confirming that ^{18}O$_2$ was from H$_2$^{18}O, and the oxygen evolution reaction could be performed by Pt/CdS@Al$_2$O$_3$. Those isotopes tracer tests identify that the Pt/CdS@Al$_2$O$_3$ is capable of overall splitting water reaction triggered in visible light irradiation.

To further confirmed the photocatalytic performance of Pt/CdS@Al$_2$O$_3$ photocatalyst, the surface microstructures after multi-cycle reaction was re-checked by XRD, XPS and DRS analyses. According to the results displayed the XRD spectrum (Fig. S11) and XPS spectrum (Fig. S12), the physicochemical properties including main phase structure and surface microstructures have no obvious change before and after repeated photocatalytic reactions. These observations clearly
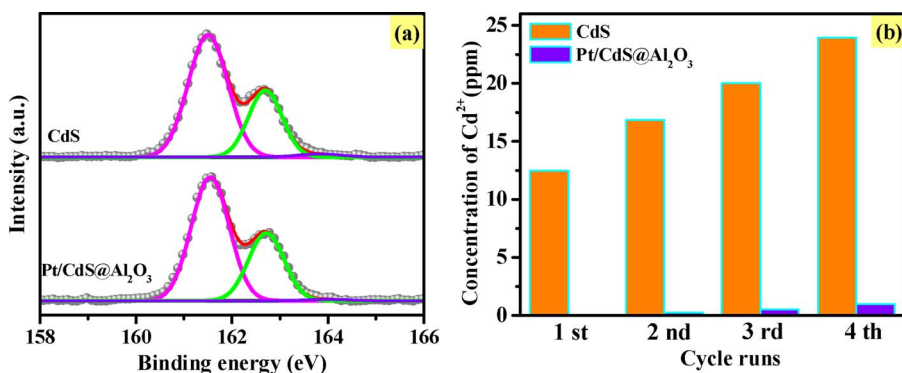
Fig. 8. (a) High-resolution XPS spectra of S 2p after photocatalytic reactions for the CdS NPs and Pt/CdS@Al$_2$O$_3$ composite, (b) the cadmium ion concentration change in solution of CdS NPs and Pt/CdS@Al$_2$O$_3$ composite with light irradiation time.

demonstrate that the core–shell Pt/CdS@Al$_2$O$_3$ catalyst has good photocatalytic stability and anti-photocorrosion capability during the photocatalytic reaction under visible light. However, it is found that the weak absorption increase in the range of 560–800 nm UV–vis spectra (Fig. S13) after photocatalytic reactions. It might due to the formation of S^0 during photocatalytic reactions [72], the result was presented in Fig. 8a. The ratio of S^0/S(total) was about 2.02% for CdS NPs itself, while S^0/S(total) was only 1.00% for Pt/CdS@Al$_2$O$_3$, indicating Al$_2$O$_3$ shell and Pt loading could inhibit thus variation.

To clarify the photocorrosion degree of the photocatalysts during reaction, ICP analysis of Cd^{2+} concentration in the reaction solutions for each run was carried out. As displayed in Fig. 8b, it was found that the concentration of Cd^{2+} had a gradual rise with the increasing irradiation time for CdS NPs. However, there was only negligible Cd^{2+} in the Pt/CdS@Al$_2$O$_3$ catalyst dispersion after several cycles, far below than that of CdS NPs. Those results confirmed the photoreaction stability of CdS NPs could be greatly improved by Al$_2$O$_3$ shell. These results agreed well with their photocatalytic performance, implying the good anti-photocorrosion performance of Pt/CdS@Al$_2$O$_3$.

In addition, to investigate the wavelength dependence of photocatalytic H$_2$ evolution, the AQE of Pt/CdS@Al$_2$O$_3$ catalyst for hydrogen evolution was estimated over a wide visible-light range of 430–550 nm. As shown in Fig. 9, it can be seen that the AQE decreases with increasing wavelengths. The highest AQE of Pt/CdS@Al$_2$O$_3$ catalyst was 0.11% at the wavelength of 430 nm for photocatalytic overall water splitting system due to the higher potential of photon [73].

3.8. The electrochemical analysis

Fig. 10a displays the periodic on/off photocurrent response of the samples under the irradiation of visible light. Apparently, for Pt/CdS@Al$_2$O$_3$ catalyst, dramatically improvements of photocurrent density than that of CdS NPs was observed, implying more efficient
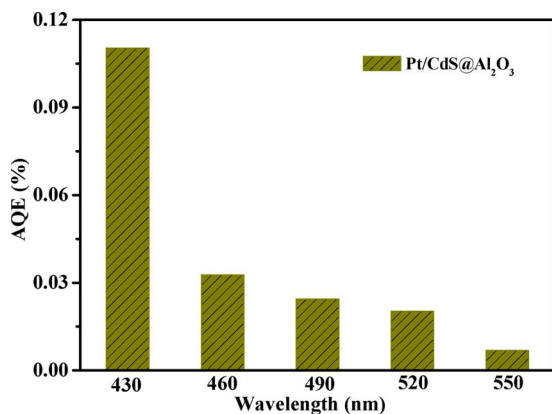

Fig. 9. The apparent quantum yield on Pt/CdS@Al$_2$O$_3$ photocatalyst under monochromatic light irradiation (λ = 430, 460, 490, 520 and 550 nm).

separation of the photogenerated electron–hole pairs and longer lifetime of the photogenerated charge carriers after Al$_2$O$_3$ coating. Furthermore, CdS NPs exhibits a decline tendency with prolonging illumination, indicating the serious photocorrosion. The photocurrent of Pt/CdS@Al$_2$O$_3$ nanocomposite remains at a relative constant value, which is in accordance with the stable of photocatalytic performance. The charge transfer and recombination process of photogenerated electrons and holes in the catalysts also be evidenced by the electrochemical impedance spectrum (EIS). The EIS is commonly composed of two partially overlapped semicircles and a straight slopping line at low frequency [74,75]. The semicircle at high frequency corresponds to charge-transfer resistance. The straight sloping line at low frequency reflects the Warburg impedance related to the diffusional effects between the active material particles and electrolyte on the interface. As depicted in Fig. 10b, Pt/CdS@Al$_2$O$_3$ composite presents a distinctly decreased diameter of the Nyquist plot than CdS NPs, implying an efficient charge-carrier transfer rate over Pt/CdS@Al$_2$O$_3$ nanocomposites. The polarization curves of CdS NPs and Pt/CdS@Al$_2$O$_3$ catalyst are displayed in Fig. 10c. The observed cathodic current in the range of −0.2 to −1.0 V can be ascribed to the H$_2$ evolution. Pt/CdS@Al$_2$O$_3$ catalyst presents an enhanced current density possessing a lower overpotential, compared with CdS NPs. The result indicates that Pt/CdS@Al$_2$O$_3$ is an excellent photocatalyst for photocatalytic H$_2$ evolution [76,77]. Mott-Schottky experiment was conducted to evaluate the band positions of the as-prepared catalysts (Fig. 10d). The slope of linear C^{-2}/E plot was positive, indicating that both CdS NPs and Pt/CdS@Al$_2$O$_3$ catalysts have an n-type semiconductor characteristic [78,79]. It can be found that CdS NPs and Pt/CdS@Al$_2$O$_3$ catalysts have the similar position of conduction band at the different frequencies. The V_{fb} of CdS NPs and Pt/CdS@Al$_2$O$_3$ both approximately equals −0.63 V vs. SCE. For many n-type semiconductors, the bottom of the conduction band was more negative by ∼0.1 V than the flat band potential [80]. Hence, the estimated positions of conduction band of CdS NPs and Pt/CdS@Al$_2$O$_3$ is −0.49 V vs NHE.

To further explore the significantly enhanced photocatalytic performances of Pt/CdS@Al$_2$O$_3$ catalyst, open circuit photovoltage decay (OCPD) measurement was performed. It is believed that OCPD technique can be utilized to assess the lifetime of photoelectrons and evaluate the recombination rate of the photo-induced electron–hole pairs. Turning on the light follows the electron accumulation, producing the negative potentials [81,82]. The V_{oc} reaches a maximum as the electron accumulation competing with the charge recombination and then attains a steady state (in Fig. 10e). Lifetime of photo-induced electron was estimated from open circuit photovoltage decay measurements by turning off illumination. Upon stopping the illumination, the V_{oc} exhibits a complex decay and can be analyzed using the approximation derived by Bisquert. The V_{oc} decay rate is closely associated with the photoelectron lifetime, as formulated by the following equation (2) [82,83].

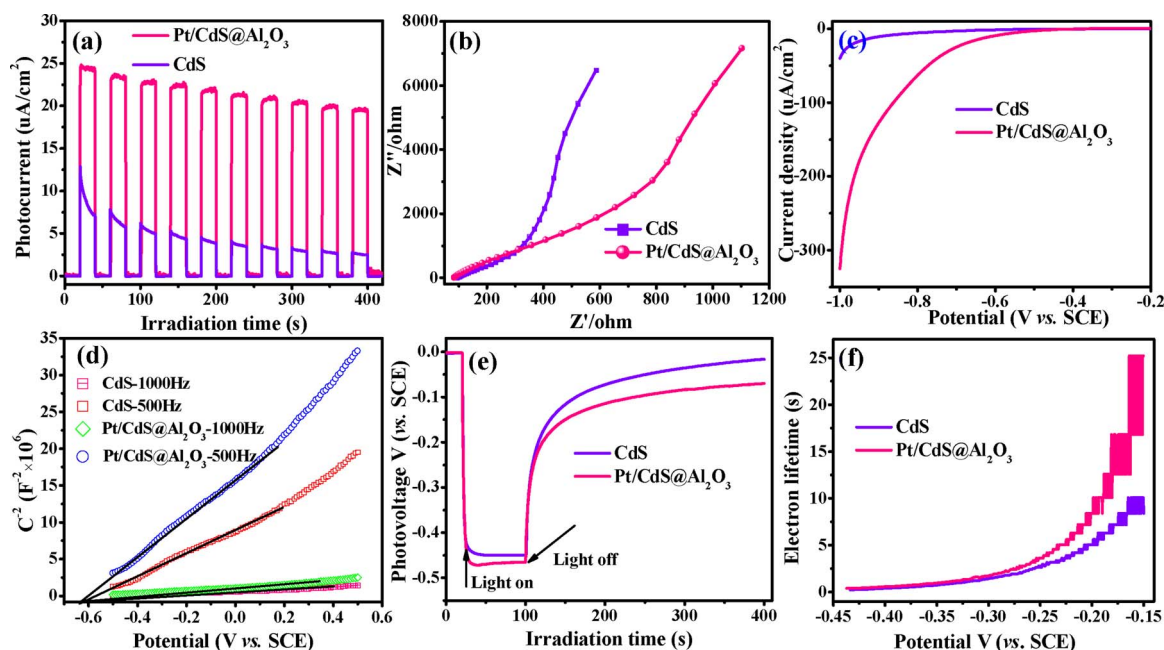$$\tau = (k_B T/e)(d\,V_{oc}/dt)^{-1} \qquad (2)$$

Fig. 10. (a) Transient photocurrent responses, (b) electrochemical impedance spectroscopy (EIS) Nyquist plots, (c) polarization curves, (d) Mott-Schottky plots, (e) illuminated open circuit potential and (f) electron lifetime determined from the decay of open circuit potential of bare CdS NPs and Pt/CdS@Al$_2$O$_3$ nanocomposites.

where τ is the potential-dependent photoelectron lifetime, k_B is the Boltzmann's constant, T is the temperature, e is the charge of a single electron, and V_{oc} is the open-circuit voltage at time t. The calculated photoelectron lifetime was shown in Fig. 10f, from which it is evident that Pt/CdS@Al$_2$O$_3$ nanocomposites demonstrate a remarkably prolonged electron lifetime in comparison with CdS NPs. Above the electrochemical results, it is concluded that the Al$_2$O$_3$ shell and Pt cocatalyst could improve the photo-induced charge separation and transfer.

The photoluminescence (PL) spectra are useful to reveal the efficiency of photogenerated charge carriers trapping, migration, transfer, separation and recombination, which are the most key factors determining the photocatalytic performance associated with semiconductor-based materials [84–96]. Fig. 11 presents the PL emission spectra of CdS NPs and Pt/CdS@Al$_2$O$_3$ catalysts at room temperature with an excitation wavelength of 420 nm. The PL intensity of the Pt/CdS@Al$_2$O$_3$ catalyst displays a considerable fluorescence decrease, compared to CdS NPs. The quench of fluorescence denotes effective separation of photogenerated electron–hole pairs, indicating excellent photocatalytic performance for Pt/CdS@Al$_2$O$_3$ catalyst. The average fluorescence lifetime results were shown in Table 2. Apparently, the
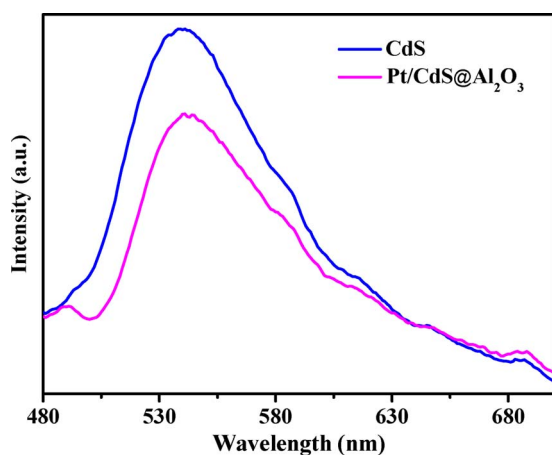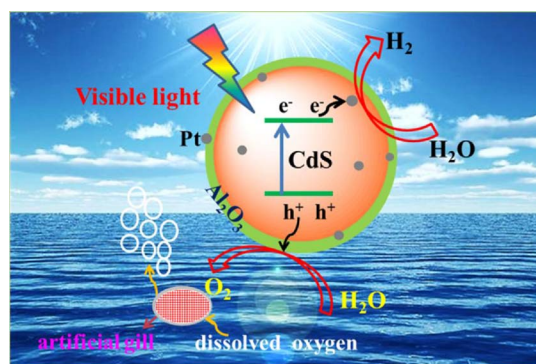
Table 2
Fluorescence lifetimes of CdS NPs, and Pt/CdS@Al$_2$O$_3$ composite.

Samples	Lifetime, τ (ns)	Pre-exponential factors B	Average lifetime, $<\tau>$ (ns)	χ^2
CdS	$\tau_1 = 8.885$ $\tau_2 = 1.535$	$B_1 = 0.133$ $B_2 = 5.814$	2.394	1.169
Pt/CdS@Al$_2$O$_3$	$\tau_1 = 14.731$ $\tau_2 = 1.877$	$B_1 = 0.045$ $B_2 = 4.511$	2.810	1.102

average lifetime of Pt/CdS@Al$_2$O$_3$ catalyst is higher than CdS NPs, which could be the effect of efficiently expediting the migration of charge carriers and inhibiting the electron–hole recombination by Al$_2$O$_3$ thin film. The above results indicate the synergetic effect of Al$_2$O$_3$ shell and Pt loading, which could boost the separation and transfer of the photogenerated electrons and eventually favoring in the higher photocatalytic efficiency of Pt/CdS@Al$_2$O$_3$ composite.

Based on the above results and characterization analysis, a reaction mechanism for photocatalytic overall water splitting over Pt/CdS@Al$_2$O$_3$ core–shell catalyst is proposed and the schematic diagram is displayed in Scheme 1. Under visible light irradiation, CdS NPs is excited to produce the electron–hole pairs, where, the photogenerated

Fig. 11. Photoluminescence (PL) spectra of the CdS NPs and Pt/CdS@Al$_2$O$_3$ composites with an excitation wavelength of 420 nm.

Scheme 1. Mechanism of overall water splitting over Pt/CdS@Al$_2$O$_3$ composite with artificial gill under visible illumination.

electrons transfer from CdS core to Pt nanoparticles, facilitating the photoactivity enhancement toward H_2 evolution. Charges can tunnel through the oxide layer by taking advantage of inner electric field in metal oxide layer [97,98], or a large number of Al^{3+} cationic vacancy network in amorphous Al_2O_3 phase [99–101]. The cationic vacancy might be also activated by trapping hole [102]. Thus, the photogenerated holes may migrate from VB of CdS to the Al_2O_3 surface producing O_2. Then, the oxygen dissolved in water would penetrate the separation membrane in artificial gill out the reaction system. Therefore, $Pt/CdS@Al_2O_3$ could realize the possibility for overall water splitting with an excellent performance.

4. Conclusion

In summary, a highly active nanocomposite photocatalyst of $Pt/CdS@Al_2O_3$ with excellent photocatalytic activity and remarkable stability has been successfully developed. The Al_2O_3 shell on the surface of the CdS core effectively protects CdS NPs from photocorrosion by rapidly transferring the interfacial photogenerated holes producing oxygen. Pt nanoparticle, as the cocatalyst, could efficiently separate photogenerated carriers and function as an active site for H_2 generation. Moreover, the utilization of artificial gill in photocatalytic overall water splitting can remove newly formed oxygen from water to prevent the oxygen leading photocorrosion and inhibit the hydrogen and oxygen recombination back to water. $Pt/CdS@Al_2O_3$ photocatalyst can achieve high efficiency for overall water splitting under visible light irradiation. This work is potential used to design and fabricate more stable and efficient CdS-based nanocatalysts for versatile solar energy conversion.

Acknowledgment

Appendix A. Supplementary data

Supplementary data associated with this article can be found, in the online version, at https://doi.org/10.1016/j.apcatb.2017.12.067.

References

[1] N.S. Lewis, Science 351 (2016) 353.
[2] G. Lu, W. Zhen, J. Mol. Catal. (China) 31 (2017) 299–304.
[3] C.S. Tain, Y.T. Liu, W.L. Sheng, J. Mol. Catal. (China) 30 (2016) 566–574.
[4] M. Grätzel, Nature 414 (2001) 338–344.
[5] P. He, Y. Chen, W.F. Fu, J. Mol. Catal. (China) 30 (2016) 269–275.
[6] T. Hisatomi, J. Kubota, K. Domen, Chem. Soc. Rev. 43 (2014) 7520–7535.
[7] L. Li, Y.P. Huang, A.Q. Zhang, J. Mol. Catal. (China) 30 (2016) 470–479.
[8] Y.Z. Xie, X. Wang, S.Q. Liu, J. Mol. Catal. (China) 30 (2016) 372–382.
[9] X. Huang, Y. Zhao, G. Lu, Z. Tang, J. Mol. Catal. (China) 31 (2017) 287–298.
[10] M.-Q. Yang, N. Zhang, M. Pagliaro, Y.-J. Xu, Chem. Soc. Rev. 43 (2014) 8240–8254.
[11] Y.Y. Cao, S.B. Huang, G.Z. Yin, J. Mol. Catal. (China) 30 (2016) 159–168.
[12] G. Lu, W. Zhang, J. Mol. Catal. (China) 31 (2017) 401–410.
[13] D. Wang, T. Hisatomi, T. Takata, C. Pan, M. Katayama, J. Kubota, K. Domen, Angew. Chem. Int. Ed. 52 (2013) 11252–11256.
[14] D. Zheng, X.N. Cao, X. Wang, Angew. Chem. Int. Ed. 55 (2016) 11512–11516.
[15] S. Chen, Y. Qi, T. Hisatomi, Q. Ding, T. Asai, Z. Li, S.S.K. Ma, F. Zhang, K. Domen, C. Li, Angew. Chem. Int. Ed. 127 (2015) 8618–8621.
[16] Q. Li, X. Li, S. Wageh, A.A. Al-Ghamdi, J. Yu, Adv. Energy Mater. 5 (2015) 1500010.
[17] A. Kudo, Y. Miseki, Chem. Soc. Rev. 38 (2009) 253–278.
[18] Y.P. Xie, Z.B. Yu, G. Liu, X.L. Ma, H.M. Cheng, Energy Environ. Sci 7 (2014) 1895–1901.
[19] K. Li, M. Han, R. Chen, S.L. Li, S.L. Xie, C. Mao, X. Bu, X.L. Cao, L.Z. Dong, P. Feng, Y.Q. Lan, Adv. Mater. 28 (2016) 8906–8911.
[20] J. Zhang, Y. Guo, Y. Xiong, D. Zhou, S. Dong, J. Catal. 356 (2017) 1–13.
[21] D. Ma, J.-W. Shi, Y. Zou, Z. Fan, X. Ji, C. Niu, L. Wang, Nano Energy 39 (2017) 183–191.
[22] N. Bao, L. Shen, T. Takata, K. Domen, Chem. Mater. 20 (2008) 110–117.
[23] C. Ye, G. Meng, Y. Wang, Z. Jiang, L. Zhang, J. Phys. Chem. B 106 (2002) 10338–10341.
[24] P. Zhao, K. Huang, Cryst. Growth Des. 8 (2008) 717–722.
[25] J. Yu, J. Zhang, M. Jaronic, Green Chem. 12 (2010) 1611–1614.
[26] M. Kimi, L. Yuliati, M. Shamsuddin, Int. J. Hydrogen Energy 36 (2011) 9453–9461.
[27] S. Xie, X. Lu, T. Zhai, J. Gan, W. Li, M. Xu, M. Yu, Y. Zhang, Y. Tong, Langmuir 28 (2012) 10558–10564.
[28] K. Ikeue, S. Shiiba, M. Machida, Chem. Mater. 22 (2010) 743–745.
[29] H.N. Kim, T.W. Kim, I.Y. Kim, S.-J. Hwang, Adv. Funct. Mater. 21 (2011) 3111–3118.
[30] S. Liu, M.-Q. Yang, Z.-R. Tang, Y.-J. Xu, Nanoscale 6 (2014) 7193–7198.
[31] L. Huang, X. Wang, J. Yang, G. Liu, J. Han, C. Li, J. Phys. Chem. C 117 (2013) 11584–11591.
[32] L.J. Zhang, S. Li, B.K. Liu, D.J. Wang, T.F. Xie, ACS Catal. 4 (2014) 3724–3729.
[33] S. Zhang, Q. Chen, D. Jing, Y. Wang, L. Guo, Int. J. Hydrogen Energy 37 (2012) 791–796.
[34] S. Shen, L. Guo, X. Chen, F. Ren, S.S. Mao, Int. J. Hydrogen Energy 35 (2010) 7110–7115.
[35] F.T. Li, Y.B. Xue, B. Li, Y.J. Hao, X.J. Wang, R.H. Liu, J. Zhao, Ind. Eng. Chem. Res. 53 (2014) 19540–19549.
[36] F.T. Li, S.J. Liu, Y.B. Xue, X.J. Wang, Y.J. Hao, J. Zhao, R. Liu, D. Zhao, J. Chem. Eur. 21 (2015) 10149–10159.
[37] A.E. Awadallah, M.S. Mostafa, A.A. Aboul-Enein, S.A. Hanafi, Fuel 129 (2014) 68–77.
[38] A. Saha, D.P. Eyman, Ind. Eng. Chem. Res. 50 (2011) 9027–9033.
[39] S.A. Al-Ghamdi, M.M. Hossain, H.I. de Lasa, Ind. Eng. Chem. Res. 52 (2013) 5235–5244.
[40] X. Ning, J. Li, B. Yang, W. Zhen, Z. Li, B. Tian, G. Lu, Appl. Catal. B 212 (2017) 129–139.
[41] E. Palomares, J.N. Clifford, S.A. Haque, T. Lutz, J.R. Durrant, J. Am. Chem. Soc. 125 (2003) 475–482.
[42] D. Zhao, C. Chen, Y. Wang, W. Ma, J. Zhao, T. Rajh, L. Zang, Environ. Sci. Technol. 42 (2008) 308–314.
[43] Y. Zhang, N. Zhang, Z.R. Tang, Y.J. Xu, Chem. Sci. 3 (2012) 2812–2822.
[44] X. Ning, S. Meng, X. Fu, X. Ye, S. Chen, Green Chem. 18 (2016) 3628–3639.
[45] M.A. Butler, J. Appl. Phys. 48 (1977) 1914–1920.
[46] J. Tang, Z. Zou, J. Ye, J. Phys. Chem. B 107 (2003) 14265–14269.
[47] J.S. Jang, S.M. Ji, S.W. Bae, H.C. Son, J.S. Lee, J. Photochem. Photobiol. A 188 (2007) 112–119.
[48] Y. Su, Z. Zhang, H. Liu, Y. Wang, Appl. Catal. B 200 (2017) 448–457.
[49] H. Liu, Z. Xu, Z. Zhang, D. Ao, Appl. Catal. B 192 (2016) 234–241.
[50] R. Chen, J. Yu, W. Xiao, J. Mater. Chem. A 1 (2013) 11682–11690.
[51] W. Wang, J. Yu, Q. Xiang, B. Cheng, Appl. Catal. B 119–120 (2012) 109–116.
[52] T. Deng, H. Liu, Green Chem. 15 (2013) 116–124.
[53] R. Peng, C.M. Wu, J. Baltrusaitis, N.M. Dimitrijevic, T. Rajhc, R.T. Koodali, Chem. Commun. 49 (2013) 3221–3223.
[54] C. Xue, T. Wang, G. Yang, B. Yang, S. Ding, J. Mater. Chem. A 2 (2014) 7674–7679.
[55] F. Ma, Y. Wu, Y. Shao, Y. Zhong, J. Lv, X. Hao, Nano Energy 27 (2016) 466–474.
[56] C.D. Wagner, D.E. Passoja, H.F. Hillery, T.G. Kinisky, H.A. Six, W.T. Jansen, J.A. Taylor, J. Vac. Sci. Technol. 21 (1982) 933–944.
[57] L.P.H. Jeurgens, W.G. Sloof, F.D. Tichelaar, E.J. Mittemeijera, Surf. Sci. 506 (2002) 313–333.
[58] J. Chaminand, L. Djakovitch, P. Gallezot, P. Marion, C. Pinel, C. Rosier, Green Chem. 6 (2004) 359–361.
[59] Y. Hu, X. Gao, L. Yu, Y. Wang, J. Ning, S. Xu, X. Lou, Angew. Chem. 125 (2013) 5746–5749.
[60] Y. Fan, M. Deng, G. Chen, Q. Zhang, Y. Luo, D. Li, Q. Meng, J. Alloys Compd. 509 (2011) 1477–1481.
[61] S. Kolhe, S.K. Kuljarni, A.S. Nigavekar, S.K. Sharma, Sol. Energy Mater. 10 (1984) 47–54.
[62] D. Barpuzary, Z. Khan, N. Vinothkumar, M. De, M. Qureshi, J. Phys. Chem. C 116 (2012) 150–156.
[63] M. Fujii, T. Kawai, S. Kawai, Chem. Phys. Lett. 106 (1984) 517–522.
[64] J.S. Jang, H.G. Kim, U.A. Joshi, J.W. Jang, J.S. Lee, Int. J. Hydrogen Energy 33 (2008) 5975–5980.
[65] H. Fujii, M. Ohtaki, K. Eguchi, H. Arai, J. Mol. Catal. A 129 (1998) 61–68.
[66] Y. Hou, A.B. Laursen, J. Zhang, G. Zhang, Y. Zhu, X. Wang, S. Dahl, I. Chorkendorff, Angew. Chem. Int. Ed. 52 (2013) 3621–3625.
[67] K. Zhang, W. Kim, M. Ma, X. Shi, J.H. Park, J. Mater. Chem. A 3 (2015) 4803–4810.
[68] B. Tian, B. Yang, J. Li, Z. Li, W. Zhen, Y. Wu, G. Lu, J. Catal. 350 (2017) 189–196.
[69] Z. Li, B. Tian, W. Zhen, Y. Wu, G. Lu, Appl. Catal. B 203 (2017) 408–415.
[70] M. Wang, Z. Li, Y. Wu, J. Ma, G. Lu, J. Catal. 353 (2017) 162–170.
[71] H. Yu, X. Huang, P. Wang, J. Yu, J. Phys. Chem. C 120 (2016) 3722–3730.
[72] M.J. Natan, J.W. Thackeray, M.S. Wrighton, J. Phys. Chem. 90 (1986) 4089–4098.
[73] S.S. Zhang, K. Xu, T.R. Jow, Electrochim. Acta 49 (2004) 1057–1061.
[74] Z. He, F. Mansfeld, Energy Environ. Sci. 2 (2009) 215–219.
[75] W. Zhen, H. Gao, B. Tian, J. Ma, G. Lu, ACS Appl. Mater. Interfaces 8 (2016) 10808–10819.
[76] W. Zhen, J. Ma, G. Lu, Appl. Catal. B 190 (2016) 12–25.
[77] X. Yang, A. Wolcott, G. Wang, A. Sobo, R.C. Fitzmorris, F. Qian, J.Z. Zhang, Y. Li, Nano Lett. 9 (2009) 2331–2336.
[78] M.W. Kanan, D.G. Nocera, Science 321 (2008) 1072–1075.
[79] A. Ishikawa, T. Takata, J.N. Kondo, M. Hara, H. Kobayashi, K. Domen, J. Am. Chem. Soc. 124 (2002) 13547–13553.
[80] Z. Zhang, P. Wang, Energy Environ. Sci. 5 (2012) 6506–6512.

[81] B.H. Meekins, P.V. Kamat, ACS Nano 3 (2009) 3437–3446.
[82] J. Bisquert, A. Zaban, M. Greenshtein, I. Mora-Seró, J. Am. Chem. Soc. 126 (2004) 13550–13559.
[83] Y. Zhang, N. Zhang, Z.-R. Tang, Y.-J. Xu, Phys. Chem. Chem. Phys. 14 (2012) 9167–9175.
[84] W.L. Zhen, X.F. Ning, B.J. Yang, Y.Q. Wu, Z. Li, G.X. Lu, Appl. Catal. B 221 (2018) 243–257.
[85] B. Tian, W. Gao, X.Q. Zhang, Y.Q. Wu, G.X. Lu, Appl. Catal. B. 221 (2018) 618–625.
[86] Z. Li, B. Tian, W.L. Zhen, W.Y. Zhang, X.Q. Zhang, Y.Q. Wu, G.X. Lu, Appl. Catal. B 219 (2017) 501–510.
[87] W.L. Zhen, W.J. Jiao, Y.Q. Wu, H.W. Jin, G.X. Lu, Catal. Sci. Tech. 7 (2017) 5028–5037.
[88] X.Q. Zhang, B. Tian, W.L. Zhen, Z. Li, Y.Q. Wu, G.X. Lu, J. Catal. 354 (2017) 258–269.
[89] W. Gao, W.Y. Zhang, G.X. Lu, Appl. Catal. B. 212 (2017) 23–31.

[90] B. Tian, Z. Li, W.L. Zhen, X.Q. Zhang, G.X. Lu, J. Catal. 352 (2017) 572–578.
[91] W.Y. Zhang, S.L. Yang, J. Li, W. Gao, Y.B. Deng, W.P. Dong, C.J. Zhao, G.X. Lu, Appl. Catal. B. 206 (2017) 89–103.
[92] Z. Li, B. Tian, W.Y. Zhang, X.Q. Zhang, Y.Q. Wu, G.X. Lu, Appl. Catal. B 204 (2017) 33–42.
[93] C. Kong, S.X. Min, G.X. Lu, Chem. Commun. 50 (2014) 9281–9283.
[94] Z. Li, C. Kong, G.X. Lu, J. Phys. Chem. C 120 (2016) 56–63.
[95] Y.Q. Wu, G.X. Lu, S.B. Li, J. Photochem. Photobiol. A 181 (2006) 263–267.
[96] F. Xiao, J. Phys. Chem. C 116 (2012) 16487–16498.
[97] A.Q. Jiang, H.J. Lee, G.H. Kim, C.S. Hwang, Adv. Mater. 21 (2009) 2870–2875.
[98] R. Jansen, J.S. Moodera, Phys. Rev. B 61 (2000) 9047.
[99] P.S. Liu, K.M. Liang, S.R. Gu, Corr. Sci. 43 (2001) 1217–1226.
[100] E. Schumann, Oxid. Met. 43 (1995) 157–172.
[101] J.P. Richters, T. Voss1, D.S. Kim, R. Scholz, M. Zacharias, Nanotechnology 19 (2008) 305202.
[102] G. Dingemans, W.M.M. Kessels, J. Vac. Sci. Technol. A 30 (2012) 040802.